Supplemental Information

Constant Growth Rate Can Be Supported by Decreasing Energy Flux and Increasing Aerobic Glycolysis

Nikolai Slavov, Bogdan Budnik, David Schwab, Edoardo Airoldi, and Alexander van Oudenaarden

Correspondence should be addressed to: nslavov@alum.mit.edu

This PDF file includes:

Experimental Design

All experiments described in the paper used a prototrophic diploid strain (DBY12007) with a S288c background and wild type HAP1 alleles, MAT**a**/MATα $HAP1^{+}$, first derived by Hickman and Winston (2007). We grew our cultures in a commercial bioreactor (LAMBDA Laboratory Instruments) using minimal media with the composition of yeast nitrogen base (YNB) and supplemented with $2g/L$ D-glucose. Before inoculation, the reactor was filled with 2L of minimal media warmed up to a working temperature of $30^{o}C$ and after reaching a steady-state of temperature and media aeration for a few hours, the oxygen and the carbon dioxide sensors were calibrated. After

calibration, oxygen and the carbon dioxide data were collected for at least 3 hours to ensure that the readings were stable, not changing.

Then cultures were started by inoculating the media with 100 μl overnight culture from DBY12007. The overnight cultures were prepared by first streaking frozen DBY12007 on YPD plates (YPD; 10 g of Bacto-Yeast extract, 20 g of Bacto-peptone, 20 g of Bacto-agar, and 20 g of glucose in 1000 ml of water) and then growing a single colony in the same minimal media used for the subsequent growth experiment in the bioreactor. The density of the culture used for inoculation was 2×10^7 cells per ml, resulting in initial density of 10^3 cells/ml for the culture in the reactor. The cultures were grown at 30^oC and continuously stirred to ensure their homogeneity. The culture was aerated with air coming from a compressed gas cylinder (Airgas, AI-B300 breathable air). The incoming flow of air was controlled by a thermal-based mass-flow controller and filtered through a $0.2\mu m$ filter to ensure sterility.

Sampling

To take samples without disturbing the cultures, we used a metal tube attached to a silicon tubing and a syringe. The metal tube could be inserted in and out of the cultures, and the syringe used to sample the required volume quickly from the homogeneous cultures. The sampling tubing was kept sterile and no culture was left in it after sampling. The volume of each sample was recorded and taken into account as necessary for estimating metabolic rates on a per cell basis. All samples were immediately processed as described in the subsections below.

Measuring of Culture Biomass

We used 3 methods to measure biomass. A single cell measurement of cell density was performed on Beckman-Coulter Multisizer 4 by counting of at least 20,000 single cells (Slavov et al., 2011; Bryan et al., 2012). Biomass density was also measured by the optical density at 600 nm (OD600) on a Hitachi U-1800 spectrophotometer and by measuring the grams of dry weight (gDW) of yeast cells. For dry weight measurements, culture samples (between 10 and 50 ml depending on cell

density) were filtered through pre-weighed filters (pore size of 0.22 μm). The filters with the cells were dried in a microwave oven and weighed every 5 min until the weight stabilized. The gDW/ml is estimated as the difference in the weight of the filter with and without the dried cells normalized to the volume of the filtered culture.

Two liters of well-aerated and well-stirred minimal medium containing 11.11 mM glucose as a sole source of carbon and energy were inoculated to a cell density of 1000 cells/ml (Figure 1A). After 10 hours (h), the culture reached a cell density allowing bulk measurements and was continuously sampled. During the first $10\ h$ of sampling (6 doubling periods, the pink region in Figure 2A-B), the biomass and the cell density increased exponentially with time, indicating a constant growth rate ($\mu = 0.4\ \ h^{-1}$) and cell division cycle (CDC) period ($1.7\ h$). Subsequently, the CDC period remained constant at $1.7\ h$ for 3 more doublings while cell-size and thus growth rate declined, dark pink region in Figure 2A-B. In fact, the doubling time remained constant until the median cell volume dropped by 3-fold and both cell growth and division stopped suddenly and completely (Figure 2C). Then the cells resumed growth (purple region in Figure 2A-B) supported by the ethanol accumulated during the first growth phase. Notably, during the second growth phase, biomass increased exponentially, indicating again a constant but much slower growth rate $\mu = 0.04\ h^{-1}$. Thus, our experimental design provides two phases of exponential growth, characterized by different carbon sources and growth rates. The transition between the two phases has been studied extensively (Brauer et al., 2005; Zampar et al., 2013) and we will not address it; rather, we focus only on the phases with constant doubling times.

Estimating O_2 Consumption and CO_2 Production

The schematic diagram for measuring oxygen consumption and carbon dioxide production is shown in Figure 1A. The air aerating the culture comes from a compressed-air bottle and has known concentrations of carbon dioxide ($C_{in}^{CO_2} = 0.04\%$) and of oxygen ($C_{in}^{O_2} = 20.94\%$). The remainder is nitrogen ($C_{in}^{N_2} = 78.08\%$), argon ($C_{in}^{Ar} = 0.93\%$) and trace gases (mostly neon) below 0.002%. We can set the rate of air entering the culture (J_{in}, $[L/h]$) and measure the concentrations of carbon dioxide (using infra-red spectroscopy) and of oxygen (using zirconia galvanic cell) leaving the reactor every second during the experiment, $C_{out}^{CO_2}(t)$ and $C_{out}^{O_2}(t)$ respectively. Based on these data and using mass-conservation, we want to estimate the rate of O_2 consumption and the rate of CO_2 production.

Estimating the Off-gas Flux

Because the volume of produced CO_2 can be different from the volume of consumed O_2, the total volume of the gas leaving the reactor per second can be slightly smaller or larger than the total volume entering the reactor per second. Since yeast do not consume or produce argon and nitrogen, we can use our measurements to compute the flux of air leaving the reactor every second, $J_{out}(t)$, as follows:

- The concentration of the inert gases (nitrogen and argon) in the incoming air is: $C_{in}^{inert} = 100 - C_{in}^{CO_2} - C_{in}^{O_2} = C_{in}^{Ar} + C_{in}^{N_2} = 0.9\% + 78.08\% = 78.98\%$.

- The concentration of the inert gases (nitrogen and argon) in the gas leaving the reactor is: $C_{out}^{inert} = 100 - C_{out}^{CO_2} - C_{out}^{O_2}$.

- Since yeast do not consume or produce nitrogen and argon, the change (if any) in the concentrations of these inert gases between the air entering the reactor (C_{in}^{inert}) and the gas leaving the reactor (C_{out}^{inert}) must be due to a change in the volume of gas leaving the reactor per unit time. Mass conservation requires that $C_{in}^{inert} J_{in} \equiv C_{out}^{inert} J_{out}$, and thus we compute flux of

gas leaving the reactor as:

$$J_{out}(t) = J_{in}\frac{C_{in}^{inert}}{C_{out}^{inert}(t)} = J_{in}\frac{100 - C_{in}^{CO_2} - C_{in}^{O_2}}{100 - C_{out}^{CO_2}(t) - C_{out}^{O_2}(t)} \tag{1}$$

In our experiments J_{in} is generally large relative to the gases consumed and produced by our cultures, resulting in small changes in the concentrations of carbon dioxide and oxygen, and thus J_{out} differs only slightly from J_{in}.

Accounting for Buffering

The application of mass conservation to our data allows us to compute the fluxes of oxygen and carbon dioxide, Ψ_{O_2} and Ψ_{CO_2} respectively, based on equations (2-3). To convert these fluxes into units of moles per hour (mol/h), we divide them by the molar volume (V_m) of air at the lab temperature (25^oC) and pressure (1 atmosphere), ($V_m = 24.47\ dm^3/mol$).

$$\Psi_{O_2} = \frac{1}{V_m}\left[J_{in}C_{in}^{O_2} - J_{out}C_{out}^{O_2}\right] \tag{2}$$

$$\Psi_{CO_2} = \frac{1}{V_m}\left[J_{in}C_{in}^{CO_2} - J_{out}C_{out}^{CO_2}\right] \tag{3}$$

The Ψ fluxes are primarily due to the gases consumed and produced by the cells. However, Ψ are also affected, to a much smaller extent, by the buffering reaction of the growth medium and the air present in the reactor and the tubing system carrying the exhaust gas to the detectors. Since we have precise measurements for the physical characteristics of our system, we can compute the contribution of the buffering according to equations (4-5) and subtract it, if necessary, to obtain a better estimate of fluxes due only to cellular metabolism.

$$\text{Buffering}^{O_2} = \frac{\partial C_{out}^{O_2}}{\partial t}\left[\underbrace{k_H^{O_2} V_{\text{medium}}}_{\text{Medium}} + \underbrace{\frac{1}{V_m} V_{\text{Air}}}_{\text{Air}}\right] \tag{4}$$

$$\text{Buffering}^{CO_2} = \frac{\partial C_{out}^{CO_2}}{\partial t}\left[\underbrace{k_H^{CO_2} V_{\text{medium}}}_{\text{Medium}} + \underbrace{\frac{1}{V_m} V_{\text{Air}}}_{\text{Air}}\right] \tag{5}$$

Where $k_H^{O_2}$ and $k_H^{CO_2}$ are the Henry's constants at 1 atmosphere pressure for oxygen and carbon dioxide respectively, with values $k_H^{O_2} = 1.3 \times 10^{-3}\ mol/L$ and $k_H^{CO_2} = 3.4 \times 10^{-2}\ mol/L$. V_{Medium} and V_{Air} are the volume of the culture (growth medium) and the volume of the air in the reactor and the tubing system. In the conditions of our experiments, the contribution of the buffering is quite small relative to the fluxes due to cellular metabolism. The terms due to the air in the reactor and the tubing are small because the volume of air is small relative to the volume of the culture; typically, the volume of air in the system is an order of magnitude smaller than the culture volume. The term due to dissolved oxygen is also very small because oxygen has low solubility in water $k_H^{O_2}$. The largest buffering term is due to the dissolved carbon dioxide and even it is quite small relative to the total flux due to cellular metabolism. When the changes in the concentrations of carbon dioxide and oxygen are small relative to J_{in}, their time derivatives are small too, and thus equations (4-5) indicate that the contribution of the buffering is going to be rather small too.

Empirical Validation of Measured O_2 and CO_2 Fluxes

We used a series of control experiments to test the estimates based on the above steps. These experiments used the same growth media as the media used for the experiments and included switching the incoming gas aerating the reactor from air to medical atmosphere (air containing $5\%\ CO_2$) or nitrogen and back. For each switch, we collected data continuously and used them to test and validate the buffering estimates based on equations (4-5). Importantly, none of the results

in the main paper depend on the small corrections for buffering.

Measuring oxygen consumption at low biomass density is exceedingly challenging since the cells consume a very small fraction of the oxygen passing through the reactor and even relatively small errors in the oxygen concentration can have a large impact on the estimated oxygen consumption. To evaluate whether our experimental setup can estimate oxygen consumption in such regime of low biomass, we conducted control experiments.

The first control experiment designed specifically to address the accuracy of flux measurements at low biomass densities was identical to the experiment described in the paper except for the carbon source: instead of 11.11 mM glucose, the media contained 100 mM ethanol as a sole source of carbon and energy (Slavov and Botstein, 2011). The complete oxidation of an ethanol molecule requires 3 O_2 molecules and produces 2 CO_2 molecules. Thus, chemical stoichiometry and mass-conservation require that the respiratory quotient (RQ, defined as the molar ratio of produced CO_2 and consumed O_2) for ethanol oxidation equals 2/3, providing a strong benchmark for evaluating the accuracy of our measurements in conditions as close as possible to these used for the experiments described in the paper. Of course, cells growing on ethanol as a sole source of carbon and energy can either have a new synthesis or degradation of reserved carbohydrates (trehalose and glycogen) which would result in small deviation of the RQ from the 2/3 expected for oxidizing ethanol. The results of this experiment (Figure 1B) indicate that the experimentally measured RQ equals the expected RQ (2/3) both at low biomass density (lower than in Figure 2) and across over 7 doubling periods corresponding to over 2 orders of magnitude in the dynamical ranges of the measured gases. Thus, increase of O_2 consumption and CO_2 production does not bias our experimental estimates of these fluxes and the respiratory quotient.

The second control experiment was designed specifically to address the accuracy of flux measurements at low biomass densities with glucose as the sole carbon source to better control for our main experiments. The experiment was identical to the experiment described in the paper except for a 40 fold lower concentration of the carbon source: instead of 2g/L (11.11 mM) glucose, the media contained 50mg/L (278 mM) glucose as a sole source of carbon and energy. With this exper-

iment we aimed to further evaluate the accuracy of our flux measurements at even lower biomass and in media having the same carbon source (glucose) as the one used in our experiments. We took advantage of the well established observation that when budding yeast is grown at very low glucose levels for long periods of time, it mostly oxidizes glucose to CO_2 and H_2O and only a very small fraction of the glucose is fermented to ethanol (Küenzi and Fiechter, 1969; Hoek et al., 1998; van Hoek P et al., 2000). The results of this experiment (Figure 1) indicate that the experimentally measured RQ remains constant over several doubling times and equals the expected RQ (1.2) for the experimental levels of glucose and growth rate (Küenzi and Fiechter, 1969; Hoek et al., 1998; van Hoek P et al., 2000).

These control experiments establish that our experimental system is able to measure the expected RQ values at low biomass densities. Furthermore, the estimated RQ values remain constant over many doubling times and several orders of magnitude change in biomass density and O_2 and CO_2 fluxes. Therefore, we conclude that while low biomass density presents a formidable challenge to measuring metabolic fluxes and RQ, our experimental design has overcome these challenges; the increase in RQ in Figure 3 is unlikely to be an artifact of the low biomass density or simply the increase of the measured fluxes of O_2 and CO_2.

Controlling for Oxygen Limitation

Oxygen limitation in the course of our experiments is an important factor to control for. We measured dissolved oxygen in the media with a Clark electrode and the dissolved oxygen always followed the oxygen levels in the exhaust gas, remaining above 80 % oxygen saturation at all times and above 90 % oxygen saturation during the first exponential phase when oxygen consumption per cell decreases. Furthermore, we performed independent experiments with different levels of aeration (varying over 8 fold dynamical range) and computed the same fluxes of oxygen, further corroborating that oxygen limitation was not a factor influencing our results.

Estimating ATP Flux

The total rate of ATP production (Ψ_{ATP}) can be estimated as a sum of the ATP produced by oxidative phosphorylation in the mitochondria and the ATP produced by fermenting glucose to ethanol. The rate of ATP produced by oxidative phosphorylation equals the flux of oxygen consumption times the number of ATP molecules generated per oxygen atom consumed, known as P/O ratio. Since the P/O ratio is hard to measure *in vivo*, multiple P/O ratios have been reported (Sheldon et al., 1996; Campbell et al., 1985; Hinkle, 2005). We used values (low limit $P/O = 1$ and high limit $P/O = 2.2$) encompassing the reported range. In addition, each completely oxidized molecule of glucose generates 2 ATPs from glycolysis and 2 GTPs, which are the equivalent of 2 ATPs, from substrate level phosphorylation during the tricarboxylic acid cycle. The rate of ATP produced by fermentation equals the flux of ethanol production, which is equivalent to the flux of CO_2 minus the flux of O_2, times 1 molecule of ATP produced by substrate level phosphorylation in the process. Thus, the total ATP flux (Ψ_{ATP}) was estimated from the fluxes of carbon dioxide (Ψ_{CO_2}) and oxygen (Ψ_{O_2}) according to: $\Psi_{ATP} = (P/O + 1/3) \times 2 \times \Psi_{O_2} + 1 \times (\Psi_{CO_2} - \Psi F_{O_2})$.

The above estimate accounts for the two main sources of ATP, glycolysis and oxidative phosphorylation, whose absolute rates we have measured directly and used for computing the ATP flux. In addition, small amounts of ATP could be released by biosynthetic reactions. Since the rate of biosynthesis is constant during the period of exponential growth considered in our analysis, these small sources can contribute at most a small constant term, which cannot account for the trend in the ATP flux that we observed (Figure 3). The conclusion that the ATP flux decrease does not depend on the exact values that we use for the efficiency of fermentation and oxidative phosphorylation: since since O_2 consumption per cell decreases (Figure 2F) and CO_2 production per cell remains steady or decreases slightly (Figure 2G), any positive efficiencies of fermentation and respiration will result in a declining ATP flux.

Mass Balance of Carbon

We sought to cross-check our measurements of metabolic fluxes (O_2, CO_2, and glucose) and of cell biomass by evaluating, at each time point of the first phase of exponential growth, whether the uptake of carbon equals its secretion and incorporation into biomass. This analysis allows using mass-conservation to evaluate the error in the data. The flux of consumed carbon (F^C_{in}) should equal the total flux of secreted carbon (F^C_{out}). Since glucose is the sole carbon source in our experiments F^C_{in} equals the flux of carbon intake from glucose (equation 6). F^C_{out} can be estimated from its major components, the fluxes of respiration ($F^C_{respiration}$), fermentation ($F^C_{fermentation}$), and biomass incorporation ($F^C_{biomass}$) according to equation 7. The estimation of these fluxes and their balance is described in the subsections below and shown in Figure 3.

$$F^C_{in} = F^C_{glucose} \tag{6}$$

$$F^C_{out} = F^C_{respiration} + F^C_{fermentation} + F^C_{biomass} \tag{7}$$

All fluxes ($F^C_{process}$) represent millimoles (mmol) of carbon per hour from the subscripted process.

Flux of Glucose and Carbon Consumption

To estimate the glucose consumption, we measured the residual glucose concentration in triplicate (using R-biopharm enzymatic kit) in the growth medium in the course of our experiment (Figure 3). The derivative of this measured time-series data equals the rate (flux) of glucose consumption. Since glucose is the sole source of carbon in our medium and each molecule of glucose has 6 carbon atoms, the flux of carbon consumption ($F^C_{glucose}$) equals 6 times the flux of glucose consumption.

Flux of Carbon Secretion and Biomass Incorporation

Since the oxidation of a glucose molecule requires 6 molecules of O_2 and produces 6 molecules of CO_2, the respiratory flux ($F^C_{respiration}$) equals the flux of oxygen consumption (Figure 2). The flux of carbon released via fermentation ($F^C_{fermentation}$) can be estimated both from the measured ethanol concentrations (Figure 3) as 3/2 the carbon released with the ethanol flux or as 3 times the flux of CO_2 due to fermentation, which is the total CO_2 flux minus the O_2 flux. We use the latter because of the much higher accuracy of the gas measurements, because of its greater reliance and thus check of the oxygen flux, and because of potential complications from the volatility of ethanol; the two estimates agree closely. Finally, the flux of carbon incorporated into biomass ($F^C_{biomass}$) can be estimated from the ratio of gDW over the atomic molar mass of carbon (12), times the growth rate (μ), times the carbon content of dry yeast biomass, which is measured to be $48\ \%$ (Verduyn et al., 1991; Hoek et al., 1998). Thus, $F^C_{biomass} = 0.48\frac{gDW}{12}\mu$.

The fluxes of carbon consumption (F^C_{in}) equal the fluxes of carbon secretion and biomass incorporation (F^C_{out}) computed from the data (Figure 3B), suggesting that our measurements are mutually consistent and can account for the fluxes in our experiments.

Measuring Stress Resistance

Stress resistance was measured as described previously(Slavov et al., 2012). Briefly, from each quantified time point, a sterile sample of $1\ ml$ culture was taken and split into three tubes, each containing $250\ \mu l$. The first tube (control) was kept at 30^oC and the remaining two tubes, each tube corresponding to either heat-shock or oxidative-shock, were either dropped in water bath at 48^oC or mixed with H_2O_2 to a final H_2O_2 concentration of $5\ mM$. After $10\ min$, the samples subjected to heat and H_2O_2 were removed and all samples washed several times with liquid YPD (YPD; 10 g of Bacto-Yeast extract, 20 g of Bacto-peptone, and 20 g of glucose in 1000 ml of water).

Each sample was serially diluted $1:10$ with liquid YPD into 9 dilutions spanning 9 orders of magnitude. The dilutions were spread on YPD (YPD; 10 g of Bacto-Yeast extract, 20 g of Bacto-

peptone, 20 g of Bacto-agar, and 20 g of glucose in 1000 ml of water) plates to measure viability. Colonies were counted after $36\ h$ incubation at $30\ ^oC$. For each time point, a minimum of 100 colonies were counted. The fraction of viable cells in a sample was quantified as the fraction of cells surviving the heat or the H_2O_2 exposure relative to the corresponding control, the cells that were not exposed to stress.

The colony forming units from the controlled samples are in excellent agreement with the cell densities measured by the Coulter counter, indicating that the cells in our cultures had higher than $99\ \%$ viability and that the procedure used to measure stress resistance did not result in loss of cells.

Measuring Messenger RNA Levels

The cells were harvested by vacuum filtering the samples followed by immediately freezing the cells in liquid nitrogen and then in a freezer at -80^oC. RNA for microarray analysis was extracted by the acid–phenol–chloroform method. RNA was amplified and labeled using the Agilent low RNA input fluorescent linear amplification kit (P/N 5184-3523; Agilent Technologies, Palo Alto, CA). This method involves initial synthesis of cDNA by using a poly(T) primer attached to a T7 promoter. Labeled cRNA is subsequently synthesized using T7 RNA polymerase and either *Cy3* or *Cy5* UTP. Each *Cy5*-labeled experimental cRNA sample was mixed with the *Cy3*-labeled reference cRNA and hybridized for 17 h at 60^oC to custom Agilent Yeast oligo microarrays $8 \times 44k$ having 8 microarrays per glass slide. Microarrays were washed, scanned with an Agilent DNA microarray scanner (Agilent Technologies), and the resulting TIF files processed using Agilent Feature Extraction Software version.

Measuring Protein Levels and Post-translational Modifications

For each time point we harvested at least 10^8 cells by $90\ sec$ centrifugation at $3,000 \times g$, followed by immediate freezing of the cells in liquid nitrogen and then in a freezer at -80^oC.

Extracting total protein

We used insoluble protein buffer (IPB) at pH 8.5 with the following composition: 50 mM Tris-HCl, 150 mM NaCl, 8 M urea, 2 % SDS, 1mM PMSF, 2mM DTT, 1:1000 Pierce protease inhibitors. The IPB was made fresh just before each use.

The cell pellet from each time-sample was suspended with $50\ \mu l$ IPB and pipeted over a metal ball cooled to a liquid nitrogen temperature in a 2 ml tube. The tubes were positioned into the PTFE 2mL tube adapter for the Retsch Mixer Mill MM400 (Retsch 22.008.0005) and the entire assembly submerged into liquid nitrogen. After the bubbling of the liquid nitrogen stopped, the assembly was mounted on the Retsch Mixer Mill MM400 and agitated for 90 seconds at 30 Hz.

The agitation was repeated 4 to 6 times and between the agitations the sample holder was returned to liquid nitrogen for cooling. Complete lysis produced fine snowy powder in the tube.

After pulverizing the cells into fine powder, the protein was dissolved by adding $450\ \mu l$ IPB and the metal ball used to pulverize the cells extracted with a magnet. The resulting $500\ \mu l$ suspension was moved to a fresh tube, span at $20,000 \times g$ for 5 minutes and the supernatant (the total protein fraction) separated for further purification by the chloroform-methanol method described below.

Chloroform–methanol Purification of Proteins

To $500 \mu l$ protein sample (about $500 \mu g$ protein) in a 15 ml falcon tube:

1. Add 2ml methanol and vortex thoroughly.
2. Add $500\ \mu l$ chloroform and vortex.
3. Add $1500\ \mu l$ water and vortex; the mixture become cloudy with precipitated protein flakes.
4. Centrifugation for 1 minute at $14,000 \times g$ resulted is three layers: a large aqueous layer on top, a circular flake of protein in the interphase, and a smaller chloroform layer at the bottom.
5. Remove top aqueous layer carefully, trying not to disturb the protein flake.
6. Add $2ml$ methanol and vortex.
7. The resulting mixture was centrifugated for 5 minutes at $20,000 \times g$, which pelleted the purified protein.
8. We removed as much methanol as possible with care since the pellet is delicate.
9. The protein pellet was dried under vacuum.

Sample Preparation

A 100 μg of total protein from each time-point-sample were digested using slightly modified FASP protocol (Wiśniewski et al., 2009). Subsequently each time-point-sample was labeled with TMT-6plex reagent (Prod # 90061, Thermo Fisher, San Jose, CA) according to a manufacturer protocol. Each set of 6 time-point-sample, labeled with the 6 distinct TMT mass tags, were pooled into one set-sample. This sample was fractionated by electrostatic repulsion-hydrophilic interaction

chromatography chromatography (ERLIC) run on an HPLC 1200 Agilent system using PolyWAX LP column (200x2.1 mm, 5 μm, 30nm, PolyLC Inc, Columbia, MD) and with a fraction collector (Agilent Technologies, Santa Clara, CA). Set-samples were fractionated into a total of 25 fractions on a $70\ min$ liquid chromatography (LC) gradient. Each ERLIC fraction was subsequently further separated by HPLC and submitted for tandem mass spectrometry analysis.

Tandem Mass Tags (TMT) Mass–spectrometry

All fractions were run on Orbitrap Velos Pro (Thermo Fisher, San Jose, CA). HPLC fractions were injected from auto-sampler into the trapping column and then eluted on capillary column ($75\ \mu m$ inner diameter $\times$ 5 cm length, packed with $5\ \mu m$ beads from Michrom Bioresources, Inc.). The fractions were eluted with a $90\ min$ gradient of acetonitrile $2 - 32\ \%$ in $0.1\ \%$ formic acid. The instrument was set to run in TOP 10 MS/MS mode method with dynamic exclusion. After MS1 scan in Orbitrap with 30K resolving power, each ion was submitted to an HCD MS/MS with 7500 resolving power and to CID MS/MS scan subsequently. All quantification data were derived from HCD spectra.

B (30

Analysis of MS Spectra

Mass/charge spectra where analyzed by MaxQuant (version 1.3.0.5) (Cox and Mann, 2008), Proteome Discover (Beta version 1.4.0.282, Thermo), Mascot (2.4, Matrix Science). Searches were performed against an yeast proteome database and common contaminants that were added to this database. Searches had trypsin enzyme specificity, allowing 2 missed cleavages. Variable modifications included in the search parameters were Met oxidation, Asn deamidation, Lys and Arg acetylation and Ser, Thr and Tyr phosphorylation. The search criteria were held at $1\ \%$ FDR on both protein and on peptide levels and $2\ \%$ for peptides with posttranslational modifications.

Measuring Cytoplasmic Amino Acid Concentrations

Analysis of underivatized amino acids was performed by liquid-chromatography tandem mass-spectrometry (LC/MS/MS) on an Agilent (Agilent Technologies, Santa Clara, CA) 6460 triple-

quadrupole LC/MS/MS system. Ions were monitored via electrospray ionization in the positive ion mode with multiple reaction monitoring (MRM). LC separations were carried out with a Phenomenex (Torrance, CA) Luna 5u SCX strong cation exchange column. For elution of the amino acids 30 mM ammonium acetate in water (solvent A) and 5% acetic acid in water (solvent B) were applied in two consecutive isocratic elution steps. An external standard curve mixture was analyzed at various concentrations $2\mu M - 200\mu M$ and used for absolute quantification. Note that we cannot distinguish Leu and Ile from their mass/charge spectra.

Analysis of Gene Regulation

The most basic question to ask from the measured mRNA and protein levels is which mRNAs and proteins change significantly (in a formal statistical sense) during the phases of exponential growth. The significance of such differences may be estimated for each time point based on the concordance of the measured levels of different peptides corresponding to the same protein (we measure on average a dozen peptides per protein) or from the null distributions estimated from biological replicas. We focused on monotonic trends in time (increasing or decreasing levels of mRNAs/proteins as a function of time) during each of the two phases of exponential growth. Such monotonic trends were quantified by two independent approaches: (i) Spearman rank correlation between the time of measuring the levels of mRNA/protein and the measured levels, resulting in correlations quantifying the trends of change and (ii) linear regression of the time of measuring the levels of mRNA/protein on the measured levels, resulting in slopes quantifying the trends of change. As a measure of goodness of fit of the linear models, we use the fraction of variance explained by the model, which for the j^{th} mRNA/protein is quantified by R_j^2:

$$R_j^2 = 1 - \frac{\sum_{i\in\alpha}(y_{ij} - f_{ij})^2}{\sum_{i\in\alpha}(y_{ij} - \bar{\mathbf{y}}_j)^2} \tag{8}$$

In (8), $\mathbf{y}_j$ is a vector of levels of the j^{th} mRNA/protein (j^{th} column in $\mathbf{Y}$), $\bar{\mathbf{y}}_j$ is its mean expression level, i is index enumerating the set of time points α used in the model and f_{ij} is the model predication for the i^{th} time point and j^{th} mRNA/protein.

For both metrics (correlations and slopes), we computed null distributions based on $20,000$ random permutations of the data. From the null distributions, we computed the probability of

observing the observed changes by chance alone (p values) and converted the p values into q values estimating the false discovery rate (FDR) to correct for multiple hypothesis testing.

Once we defined sets of genes based on the changes of their mRNAs and protein levels, we sought to identify whether some biological functions are over-represented within a set. Such analysis can be done by the widely–used gene ontology (GO) term finder (GO Term Finder (Boyle et al., 2004)). The results indicated very statistically significant enrichment for a large number of biological functions. During the first phase (Figure 4A), genes decreasing both at the mRNA and protein levels are highly ($p < 10^{-42}$) enriched for ncRNAs metabolic process, ribosome biogenesis, rRNA processing, amino acids and tRNAs processing; genes increasing at the mRNA and protein levels are enriched ($p < 10^{-20}$) for oxidation-reduction process, generation of metabolites and energy, glycogen & trehalose metabolism. During the second phase (Figure 4B), genes decreasing both at the mRNA and protein levels are highly ($p < 10^{-33}$) enriched for mitochondrial translation and organization, biosynthesis, translation, amino acids, ncRNA, rRNA; genes increasing at the mRNA and protein levels are enriched ($p < 10^{-14}$) for catabolism, oxidation-reduction process, carbohydrate metabolism, gluconeogenesis, glycolysis, and generation of metabolites and energy.

While the GO terms finder is a useful tool for identifying functional groups of genes, it has a number of drawbacks including hard thresholding, data discretization (binarization and the associated loss of information), and decreased statistical power for GO terms with a small number of genes (Slavov and Botstein, 2010). To overcome these drawbacks, we applied non–parametric statistical analysis for identifying sets of genes with statistically significant responses. This analysis makes use of prior knowledge of biological networks and metabolic pathways (or even the GO terms) to identify sets of genes. For each set, the distribution of responses (such slopes computed from regressing the mRNA/protein levels on time) of the genes that belong to the set is compared to the distribution of responses to all genes. The statistical significance of the difference between the two distributions, if any, is computed from the nonparametric Wilcoxon rank–sum (Mann Whitney) test. It is a non-parametric test for comparing two distributions without making assumptions about their shapes and gives the probability of obtaining greater observations in one population versus the other by chance alone. The null hypothesis in the rank–sum test is that both samples have the same probability of exceeding each other. We used this approach to systematically evaluate the all biochemical pathways curated by the *Saccharomyces* Genome Database (SGD). All p values were corrected for multiple hypotheses testing by converting them into q values quantifying

the false discovery rate (FDR).

Decline in Folate-mediated Mitochondrial NADPH Production and One-carbon Metabolism

The biochemical pathways with significant dynamics during phase 1 show very strong enrichment (consistent decline at both mRNA and protein level, FDR $\ll 1\%$) for folate metabolism, involved in one-carbon (methyl) transfer, and the serine hydroxymethyltransferases, generating methyl groups from the conversion of serine to glycine (Figure 4 and Figure 4). The intracellular concentrations of both serine and glycine remain constant throughout phase 1 (albeit they plummet after the di-auxie shift; Figure 5B) suggesting that the decline in serine hydroxymethyltransferases is related to the decline in producing methyl groups; this suggestion is further supported by a parallel decline in serine biosynthesis from 3-phosphoglycerate. Thus, the levels of all enzymes (and their corresponding mRNAs) catalyzing reactions mitochondrial NADPH from from 3-phosphoglycerate decline during the first phase of constant doubling time.

Inferring TF Regulation

One of simplest approaches to identifying transcription factors (TF) that might contribute to the measured transcriptional response is to compute the overlap between a set of genes with similar expression profiles, such as increasing or decreasing during the phase of constant growth rate (Figure 2 and Figure 4), and the targets of a TF as identified independently from chromatin immunoprecipitation experiments (Harbison et al., 2004; MacIsaac et al., 2006). Given a set of n genes selected based on their increase or decrease during exponential growth out of all $N = 6000$ genes and a TF regulating T target genes, the probability of observing an overlap of k genes between the two gene sets by chance alone (*p value*) is given by the cumulative mass function of the hypergeometric distribution, eq. 9:

$$P(X \geq k|N,T,n) = \sum_{i=k}^{i=T} \frac{\binom{T}{i}\binom{N-T}{n-i}}{\binom{N}{n}} = 1 - \sum_{i=0}^{i=k-1} \frac{\binom{T}{i}\binom{N-T}{n-i}}{\binom{N}{n}} \tag{9}$$

The p-values in Table 1 are computed based on the TF targets published by MacIsaac et al. (2006) at $p \leq 0.001$ and conservation level 1. Chief advantages of this approach are its simplic-

ity and the avoidance of assumptions, such as approximating TF activities with the levels of the corresponding mRNAs. This approach lacks power to identify all TFs because of the incomplete knowledge of the transcriptional network. Nonetheless, the rate of false positives is very low: A low *p value* for the overlap of the targets of the i^{th} TF and the j^{th} gene set indicates high probability that the i^{th} TF regulates the j^{th} gene set. Characterizing combinatorial regulation (Slavov and Dawson, 2009; Petti et al., 2011) and building quantitative models requires more advanced analysis, such as network inference algorithms (Markowetz and Spang, 2007; Slavov, 2010) and further experimental testing.

References

Boyle, E. I., Weng, S., Gollub, J., Jin, H., Botstein, D., Cherry, J. M. and Sherlock, G. (2004). GO::TermFinder–open source software for accessing Gene Ontology information and finding significantly enriched Gene Ontology terms associated with a list of genes. Bioinformatics (Oxford, England) *20*, 3710–3715.

Brauer, M. J., Saldanha, A. J., Dolinski, K. and Botstein, D. (2005). Homeostatic Adjustment and Metabolic Remodeling in Glucose-limited Yeast Cultures. Molecular Biology of the Cell *16*, 2503–2517.

Bryan, A., Engler, A., Gulati, A. and Manalis, S. (2012). Continuous and long-term volume measurements with a commercial coulter counter. PloS one *7*, e29866.

Campbell, S., Jones, K. and Shulman, R. (1985). In vivo ^{31}P nuclear magnetic resonance saturation transfer measurements of phosphate exchange reactions in the yeast *Saccharomyces cerevisiae*. FEBS letters *193*, 189–193.

Cox, J. and Mann, M. (2008). MaxQuant enables high peptide identification rates, individualized ppb-range mass accuracies and proteome-wide protein quantification. Nature biotechnology *26*, 1367–1372.

Harbison, C. T., Gordon, D. B., Lee, T. I., Rinaldi, N. J., Macisaac, K. D., Danford, T. W., Hannett, N. M., Tagne, J., Reynolds, D. B., Yoo, J., Jennings, E. G., Zeitlinger, J., Pokholok, D. K., Kellis,

M., Rolfe, P. A., Takusagawa, K. T., Lander, E. S., Gifford, D. K., Fraenkel, E. and Young, R. A. (2004). Transcriptional regulatory code of a eukaryotic genome. Nature *431*, 99–104.

Hickman, M. and Winston, F. (2007). Heme levels switch the function of Hap1 of Saccharomyces cerevisiae between transcriptional activator and transcriptional repressor. Molecular and cellular biology *27*, 7414–7424.

Hinkle, P. (2005). P/O ratios of mitochondrial oxidative phosphorylation. Biochimica et Biophysica Acta (BBA)-Bioenergetics *1706*, 1–11.

Hoek, P. V., Dijken, J. P. V. and Pronk, J. T. (1998). Effect of Specific Growth Rate on Fermentative Capacity of Baker's Yeast. Applied and Environmental Microbiology *64*, 4226–4233.

Küenzi, M. T. and Fiechter, A. (1969). Changes in carbohydrate composition and trehalase-activity during the budding cycle of Saccharomyces cerevisiae. Archiv Fr Mikrobiologie *64*, 396–407.

MacIsaac, K. D., Wang, T., Gordon, D. B., Gifford, D. K., Stormo, G. D. and Fraenkel, E. (2006). An improved map of conserved regulatory sites for Saccharomyces cerevisiae. BMC Bioinformatics *7*, 113–113.

Markowetz, F. and Spang, R. (2007). Inferring cellular networks–a review. BMC bioinformatics *8*, S5.

Petti, A. A., Crutchfield, C. A., Rabinowitz, J. D. and Botstein, D. (2011). Survival of starving yeast is correlated with oxidative stress response and nonrespiratory mitochondrial function. Proceedings of the National Academy of Sciences *108*, E1089 E1098.

Sheldon, J., Williams, S., Fulton, A. and Brindle, K. (1996). ^{31}P NMR magnetization transfer study of the control of ATP turnover in *Saccharomyces cerevisiae*. Proceedings of the National Academy of Sciences *93*, 6399.

Slavov, N. (2010). Inference of Sparse Networks with Unobserved Variables. Application to Gene Regulatory Networks. JMLR W&CP *9*, 757–764.

Slavov, N., Airoldi, E. M., van Oudenaarden, A. and Botstein, D. (2012). A conserved cell growth cycle can account for the environmental stress responses of divergent eukaryotes. Molecular Biology of the Cell *23*, 1986–1997.

Slavov, N. and Botstein, D. (2010). Universality, specificity and regulation of S. cerevisiae growth rate response in different carbon sources and nutrient limitations. PhD thesis, Princeton University.

Slavov, N. and Botstein, D. (2011). Coupling among growth rate response, metabolic cycle, and cell division cycle in yeast. Molecular Biology of the Cell *22*, 1997–2009.

Slavov, N. and Dawson, K. A. (2009). Correlation signature of the macroscopic states of the gene regulatory network in cancer. Proceedings of the National Academy of Sciences *106*, 4079–4084.

Slavov, N., Macinskas, J., Caudy, A. and Botstein, D. (2011). Metabolic cycling without cell division cycling in respiring yeast. Proceedings of the National Academy of Sciences of the United States of America *108*, 19090–19095.

van Hoek P, van Dijken JP and Pronk (2000). Regulation of fermentative capacity and levels of glycolytic enzymes in chemostat cultures of Saccharomyces cerevisiae. Enzyme and Microbial Technology *26*, 724–736.

Verduyn, C., Stouthamer, A., Scheffers, W. and Dijken, J. (1991). A theoretical evaluation of growth yields of yeasts. Antonie van Leeuwenhoek *59*, 49–63.

Wiśniewski, J., Zougman, A., Nagaraj, N. and Mann, M. (2009). Universal sample preparation method for proteome analysis. Nature methods *6*, 359–362.

Zampar, G. G., Kümmel, A., Ewald, J., Jol, S., Niebel, B., Picotti, P., Aebersold, R., Sauer, U., Zamboni, N. and Heinemann, M. (2013). Temporal system-level organization of the switch from glycolytic to gluconeogenic operation in yeast. Molecular systems biology *9*, 651.

Supplemental Figures and Captions

Figure 1. Rates of O_2 Consumption and CO_2 Production during Batch Growth in Media Containing $50\ mg/L$ Glucose as a Sole Source of Carbon and Energy
(A) Cell density (single cells per ml) during exponential growth on glucose.
(B) The levels of O_2 in the exhaust gas were measured continuously (every second) with ZrO_2 cell.
(C) The levels of CO_2 in the exhaust gas were measured continuously (every second) with infra red spectroscopy.
(D) Fluxes of O_2 uptake Ψ_{O_2} and CO_2 production Ψ_{CO_2} estimated from the data in (A) and (B) and eqn. 1-5.
(E) Respiratory quotient (RQ), defined as the ratio of Ψ_{CO_2} to Ψ_{O_2}.
Related to Figure 1.

Figure 2. The Growth Rate and the Doubling Period of Batch Cultures Remains Constant for 9 Generations.
(A) Yeast batch cultures growing in minimal medium were sampled every $10 - 15\ min$ and at each time-point optical density at $600\ nm$
(B) Number of cell per ml of culture.
(C) Cell size distributions plotted as a heat map indicating the percent of cells in each bin.
Related to Figure 2.

Figure 3. Concentrations of Residual Glucose and Generated ethanol in the Growth Medium. Concentrations were measured with the enzymatic R-Biopharm kits.
Related to Figure 3.

Figure 4. Global Remodeling of mRNA and Protein Regulation during Batch Growth at a Constant Growth Rate.
(A) The same time-point protein sample was labeled with different TMT tags (127 or 130) the labeled fractions mixed at $1/0.6$ ratio; The ratio in the figure is estimated empirically by regression and the correlation coefficient is computed based on all quantified peptides, $5\ 237$ in total. The color-code reflects the density of datapoints.
(B) Levels of human proteins from the dynamic universal proteomics standard (USP2). UPS2 was spiked at different levels (x-axis) in the total yeast protein extract and quantified by TMT. The levels quantified by TMT (y-axix) correspond closely to the spiked levels. The lowest spiked amount in the first channel is set to 1 for all proteins and all other levels reported as fold increase relative to the first TMT channel.
(C) Metabolic pathways and biological functions that change significantly during growth at a constant doubling time. During the phases of constant doubling periods, the dynamics of genes within a pathway, quantified by regression slopes, were compared to the time dynamics for all genes. The gene ontology (GO) terms that show significant dynamics (FDR $< 1\%$). The magnitude of change for each gene set is quantified as the average percent change in the level of its genes per doubling period of the cells.
(D) The same as in C but for biochemical pathways at FDR $< 2\%$.
Related to Figure 4.

Figure 5. Transcriptional, Metabolic and Post-translational Dynamics during Batch Growth at a Constant Rate
(A) The levels of all enzymes (and their corresponding mRNAs) catalyzing reactions of the tricarboxylic acid (TCA) cycle. Many mRNAs increase in abundance gradually but the levels of the corresponding enzymes (proteins) do not change until the very last time point, just before the growth stops. The enzymes encoded by mRNAs whose levels decease also decrease in concert with the mRNAs. The data are displayed on a $\log_2$ scale with 2 fold dynamical range.
(B) The mRNAs of hydroperoxide and superoxide-radicals induced glutathione-dependent oxidoreductases (RGX) decline during growth at a constant doubling time. The hydroperoxide and superoxide-radicals induced mRNAs coding for GRX3 and GRX4 decrease, parallel to the decreased oxygen consumption (Figure 2F), during the first exponential growth phase. Data are displayed on a $\log_2$ scale.
(C) Intracellular amino acid levels during the diauxic shift. The levels of intracellular amino acid were measured my liquid chromatography tandem mass-spectrometry (LC-MS/MS) are displayed on a $\log_2$ scale.
(D) Dynamic Changes of Acetylated Peptides during Batch Growth at a Constant Rate. The levels of hundreds of acetylated peptides, measured my liquid chromatography tandem mass-spectrometry (LC-MS/MS), are displayed on a $\log_2$ scale. The peptides are arranges based on their rate of change relative to time as computed by a linear regression. Related to Figure 5.

Figure S1

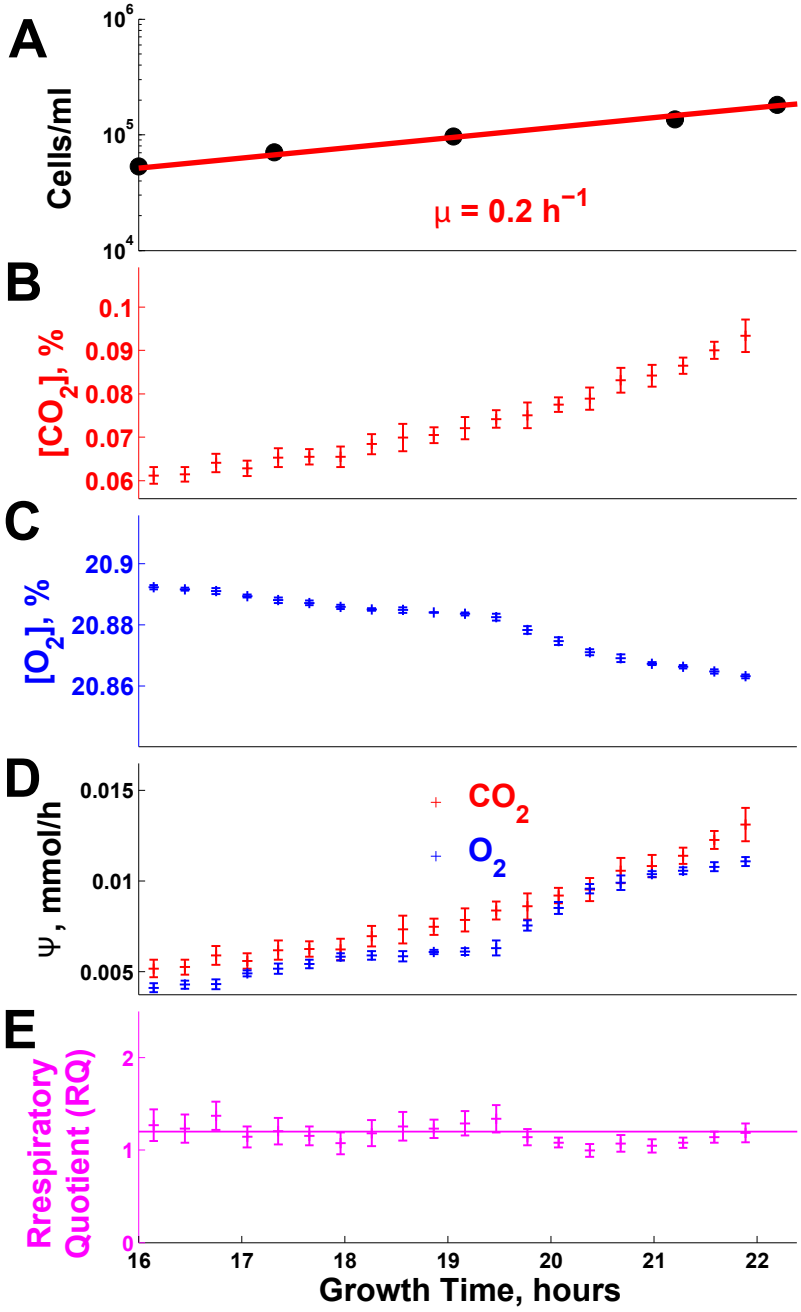
A
Cells/ml
10^6
10^5
10^4
μ = 0.2 h^{-1}
B
$[CO_2]$, %
0.1
0.09
0.08
0.07
0.06
C
$[O_2]$, %
20.9
20.88
20.86
D
Ψ, mmol/h
0.015
0.01
0.005
CO_2
O_2
E
Rrespiratory Quotient (RQ)
2
1
0
16
17
18
19
20
21
22
Growth Time, hours

Figure S2

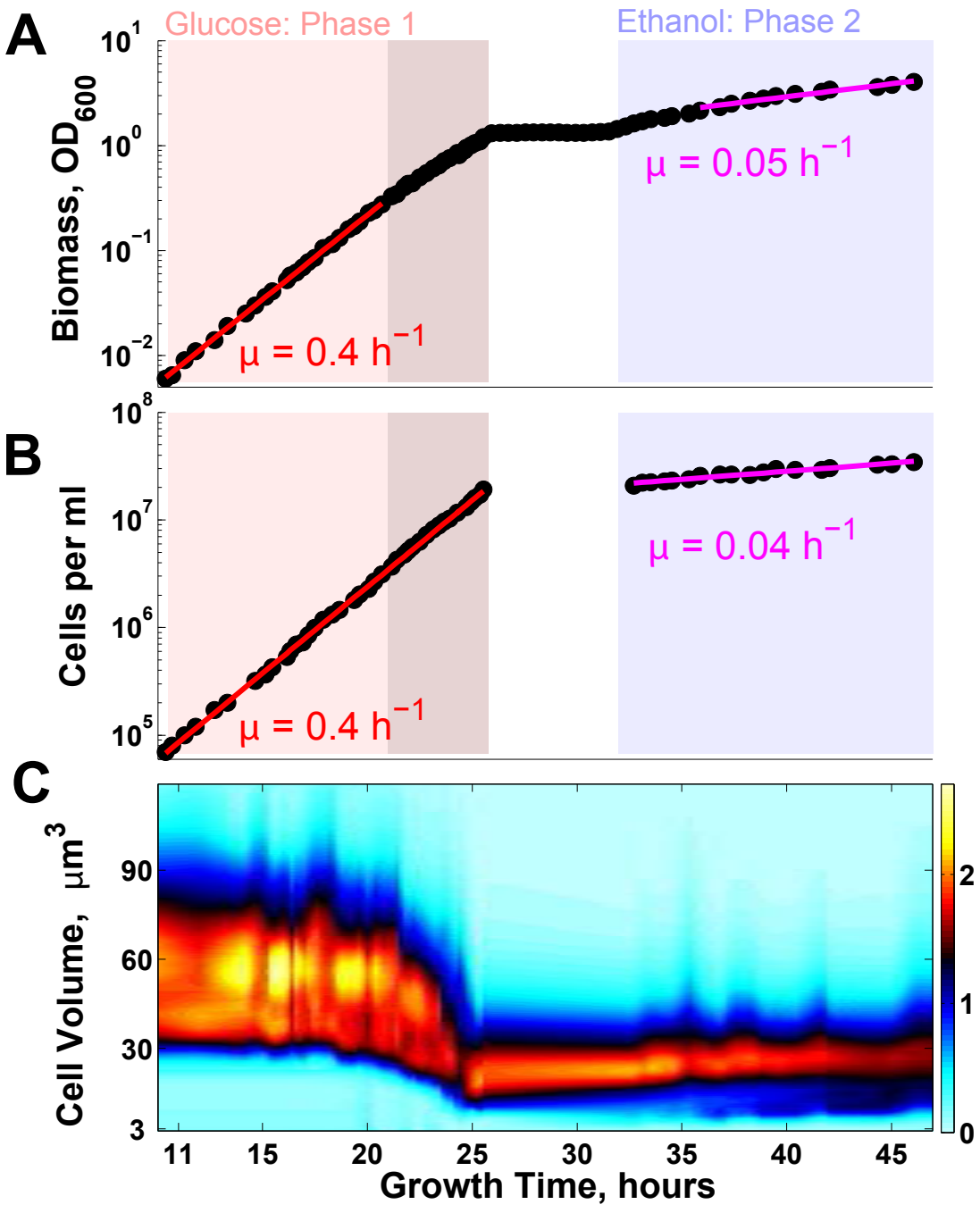
A
Glucose: Phase 1
Ethanol: Phase 2
Biomass, OD600
μ = 0.4 h−1
μ = 0.05 h−1
B
Cells per ml
μ = 0.4 h−1
μ = 0.04 h−1
C
Cell Volume, μm3
Growth Time, hours

Figure S3

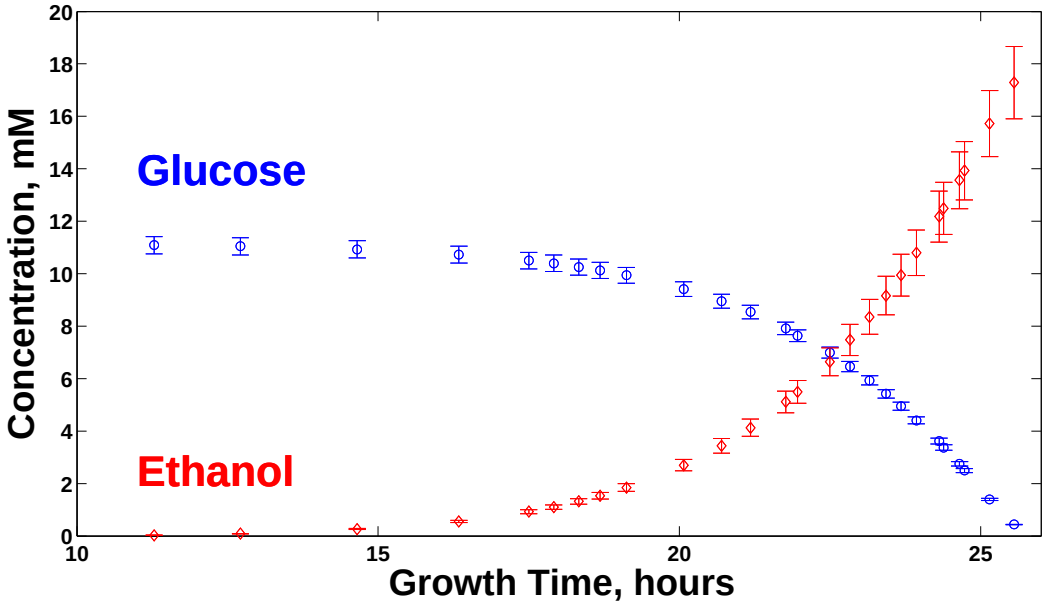
Concentration, mM
Growth Time, hours
Glucose
Ethanol
0
2
4
6
8
10
12
14
16
18
20
10
15
20
25

Figure S4

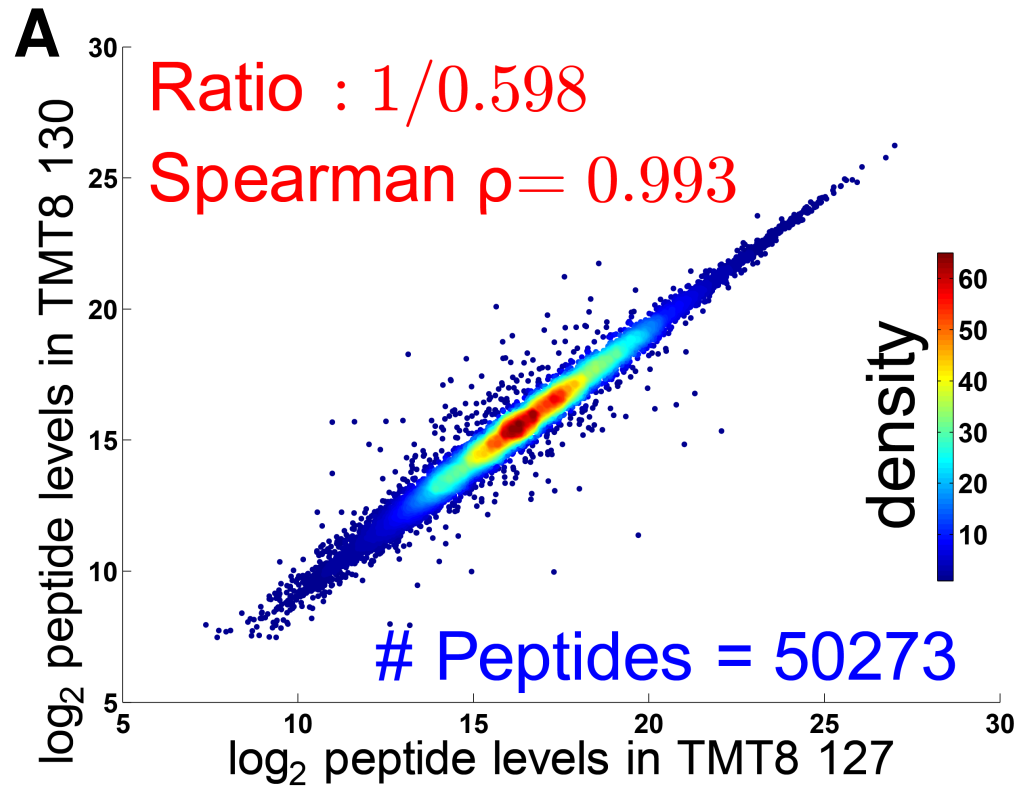
A
Ratio : 1/0.598
Spearman ρ= 0.993
Peptides = 50273
density
60
50
40
30
20
10
log2 peptide levels in TMT8 130
log2 peptide levels in TMT8 127
5
10
15
20
25
30

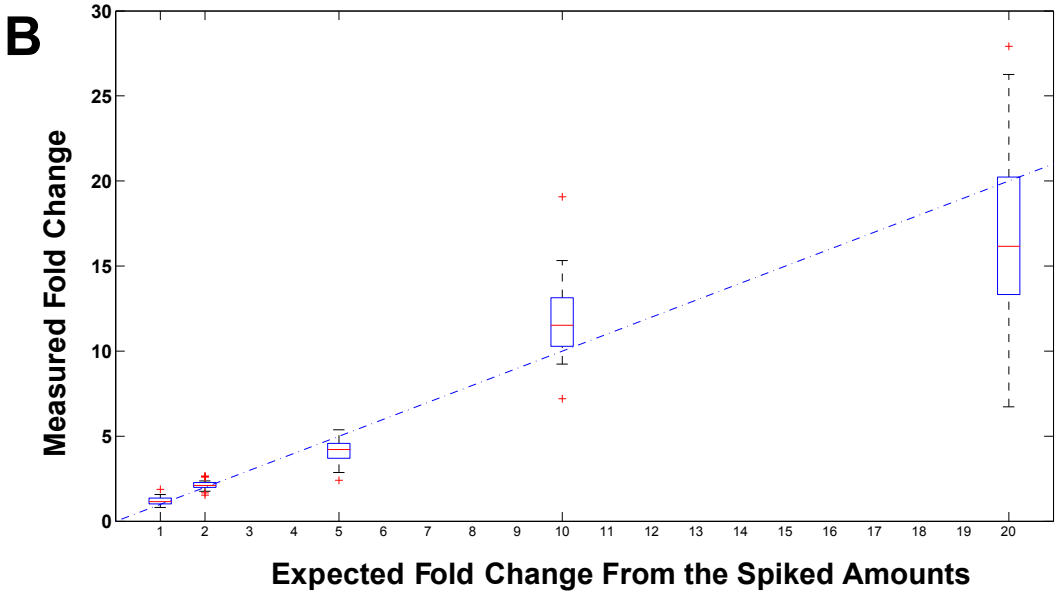
B
Measured Fold Change
Expected Fold Change From the Spiked Amounts
0
5
10
15
20
25
30
1
2
3
4
5
6
7
8
9
10
11
12
13
14
15
16
17
18
19
20

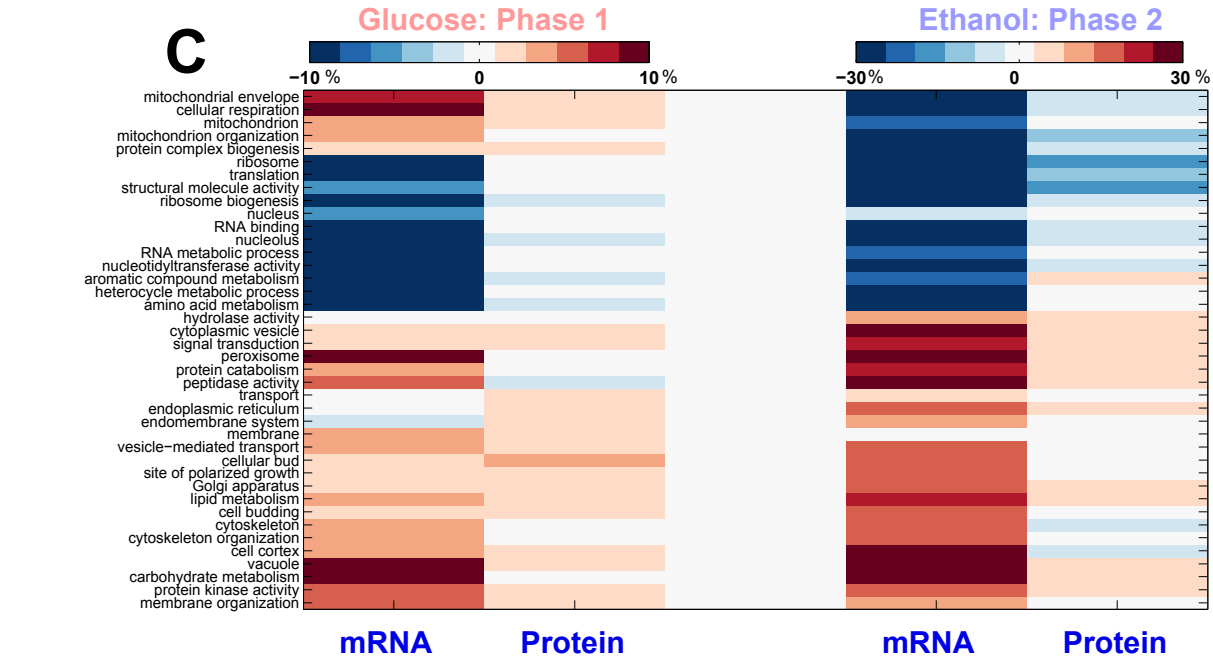
C
Glucose: Phase 1
Ethanol: Phase 2
−10 %
0
10 %
−30 %
0
30 %
mitochondrial envelope
cellular respiration
mitochondrion
mitochondrion organization
protein complex biogenesis
ribosome
translation
structural molecule activity
ribosome biogenesis
nucleus
RNA binding
nucleolus
RNA metabolic process
nucleotidyltransferase activity
aromatic compound metabolism
heterocycle metabolic process
amino acid metabolism
hydrolase activity
cytoplasmic vesicle
signal transduction
peroxisome
protein catabolism
peptidase activity
transport
endoplasmic reticulum
endomembrane system
membrane
vesicle−mediated transport
cellular bud
site of polarized growth
Golgi apparatus
lipid metabolism
cell budding
cytoskeleton
cytoskeleton organization
cell cortex
vacuole
carbohydrate metabolism
protein kinase activity
membrane organization
mRNA
Protein
mRNA
Protein

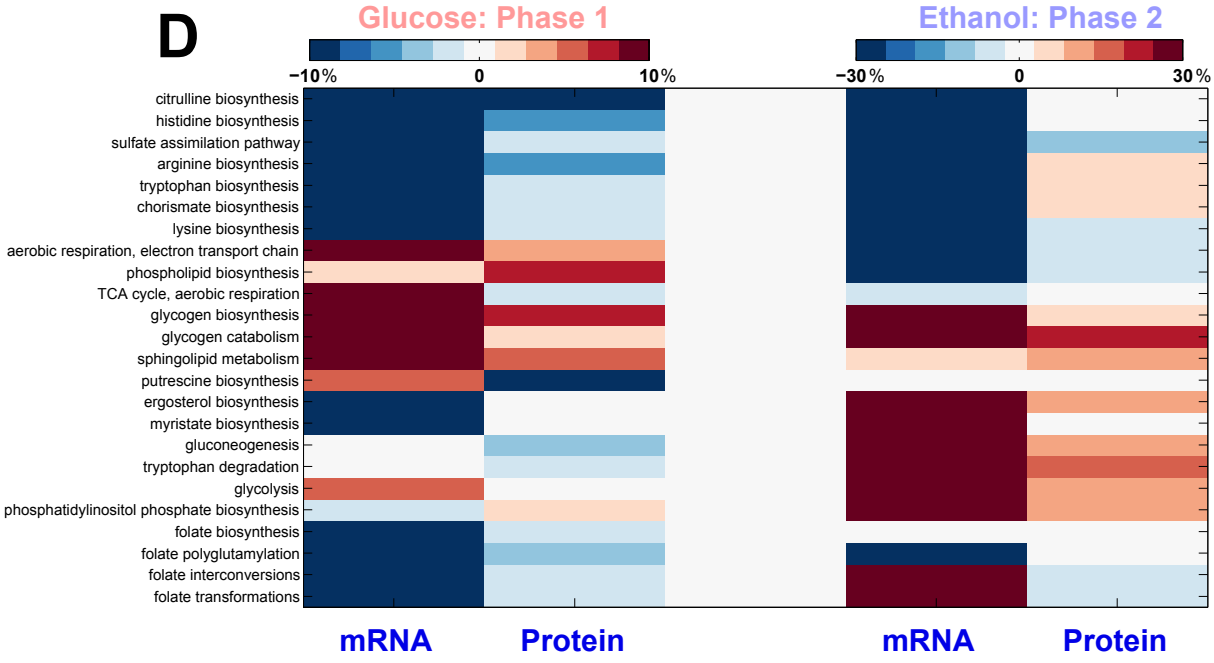
D
Glucose: Phase 1
Ethanol: Phase 2
−10 %
0
10 %
−30 %
0
30 %
citrulline biosynthesis
histidine biosynthesis
sulfate assimilation pathway
arginine biosynthesis
tryptophan biosynthesis
chorismate biosynthesis
lysine biosynthesis
aerobic respiration, electron transport chain
phospholipid biosynthesis
TCA cycle, aerobic respiration
glycogen biosynthesis
glycogen catabolism
sphingolipid metabolism
putrescine biosynthesis
ergosterol biosynthesis
myristate biosynthesis
gluconeogenesis
tryptophan degradation
glycolysis
phosphatidylinositol phosphate biosynthesis
folate biosynthesis
folate polyglutamylation
folate interconversions
folate transformations
mRNA
Protein
mRNA
Protein

Figure S5

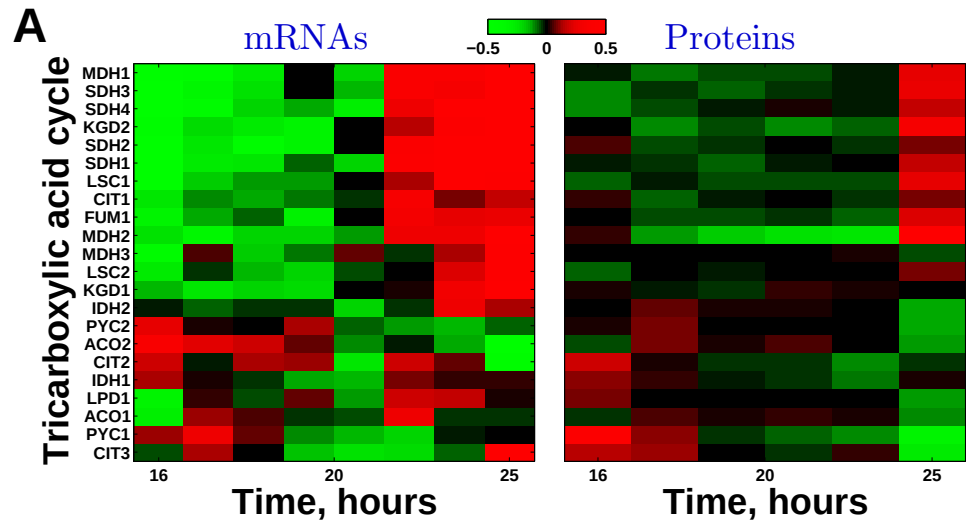
A
mRNAs
−0.5
0
0.5
Proteins
Tricarboxylic acid cycle
MDH1
SDH3
SDH4
KGD2
SDH2
SDH1
LSC1
CIT1
FUM1
MDH2
MDH3
LSC2
KGD1
IDH2
PYC2
ACO2
CIT2
IDH1
LPD1
ACO1
PYC1
CIT3
16
20
25
Time, hours
16
20
25
Time, hours

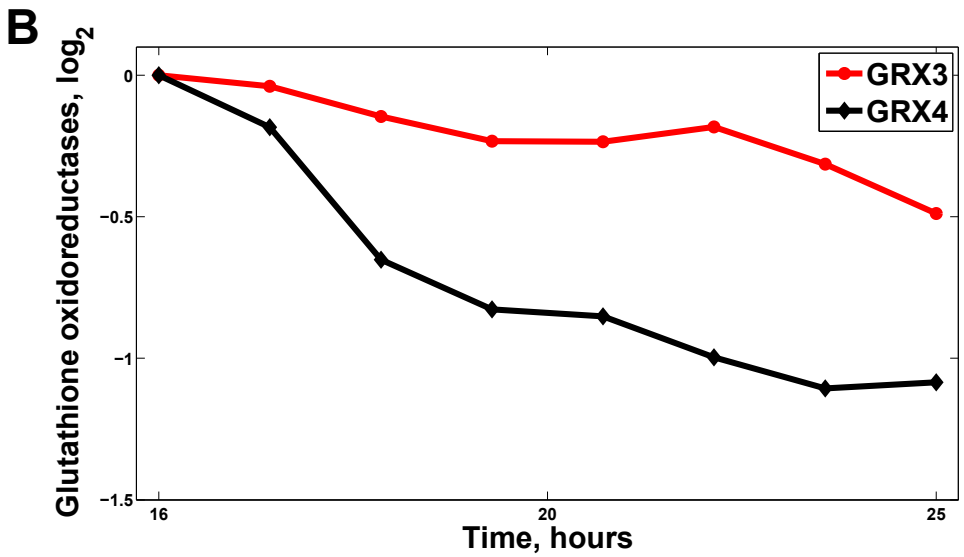
B
Glutathione oxidoreductases, log2
0
−0.5
−1
−1.5
GRX3
GRX4
16
20
25
Time, hours

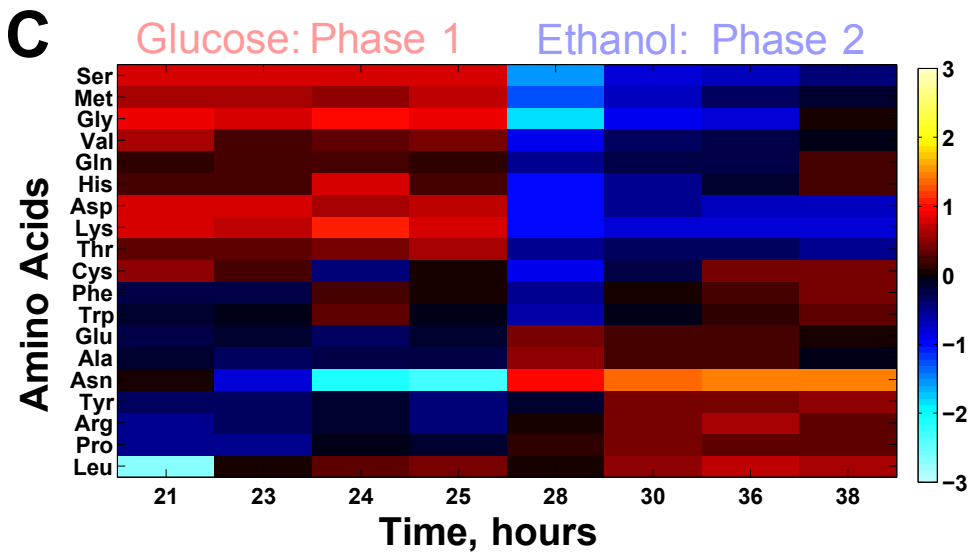
C
Glucose: Phase 1
Ethanol: Phase 2
Amino Acids
Ser
Met
Gly
Val
Gln
His
Asp
Lys
Thr
Cys
Phe
Trp
Glu
Ala
Asn
Tyr
Arg
Pro
Leu
21
23
24
25
28
30
36
38
Time, hours
3
2
1
0
−1
−2
−3

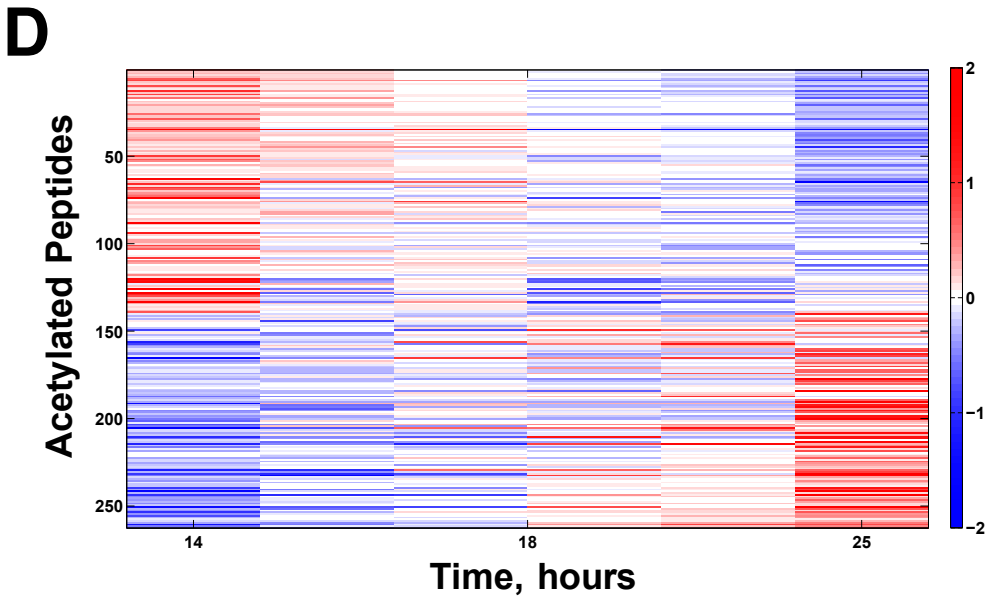
D
Acetylated Peptides
50
100
150
200
250
14
18
25
Time, hours
2
1
0
−1
−2

Table S1. Transcription factors (TF) regulating the transcriptional response during the first phase of exponential growth at a constant rate

Gene Set[a]	TF Name	# TF Target Genes[b]	# Overlapping Genes[c]	p value[d]
Repressed Genes (1356)	Gcn4p	152	74	$< 10^{-20}$
	Fhl1p	143	63	$< 10^{-9}$
	Bas1p	34	21	$< 10^{-7}$
	Met4p	11	8	$< 10^{-4}$
	Met32p	21	12	$< 10^{-4}$
	Aab1p	241	74	$< 10^{-3}$
	Gln3p	67	26	$< 10^{-3}$
	Sfp1p	32	14	$< 10^{-3}$
	Arg81p	15	8	$< 10^{-3}$
	Leu3p	21	10	$< 10^{-3}$
	Rap1p	105	37	$< 10^{-3}$
Induced Genes (1163)	Fkh2p	100	37	$< 10^{-5}$
	Msn4p	73	27	$< 10^{-4}$
	Msn2p	89	30	$< 10^{-3}$
	Aft2p	89	28	$< 10^{-3}$
	Aft1p	66	21	$< 10^{-3}$

[a]Sets of genes (number in the set shown in parentheses) whose mRNA levels either increase or decrease during the first phase of exponential growth at FDR $< 1\%$
[b]Number of genes regulated by the TF according to MacIsaac et al. (2006).
[c]Number of TF target genes found in the gene set.
[d]Probability for observing this or larger number of overlapping genes by chance.